Study on vibration mechanism induced by skidding in pure rolling contact

Chan Xu [a], Tonghai Wu [a,*], Hongbin Yang [a], Hongkun Wu [b], Ngaiming Kwok [b]

[a] *Key Laboratory of Design Science and Basic Components, Xi'an Jiaotong University, Xi'an, Shaanxi, 710049, China*
[b] *School of Mechanical and Manufacturing Engineering, The University of New South, Wales, Sydney, NSW, 2052, Australia*

ARTICLE INFO

ABSTRACT

Skidding in a rolling bearing often causes unexpected surface wear and uneven vibration. To explore the fundamental interaction mechanisms, an investigation is conducted experimentally and numerically on the tribo-dynamic responses of a simplified sliding-rolling contact. Vibration analyses show that the tangential vibration contains not only the rotational frequency of the roller but also the higher harmonics excited by the sliding-rolling contact. Surface contact stress analysis is also carried out with a twin-discs model. Results show that, with sliding occurring in the rolling contact, the unstable shear stress variation is induced and becomes the root cause of the tangential vibration. Further wear checks reveal that the wear failure under sliding-rolling contact coincides with the shear effect of contact interfaces.

1. Introduction

The rolling bearing is the major supporting component of many rotating machines for its high reliability and low friction characteristics [1]. However, skidding often occurs during the rolling motion due to the change in the operating conditions and thus causes uneven vibration and wear failure. Based on the primary theories of the sliding-rolling contact, the excited vibration and wear behaviour have been independently studied over the decades. However, the interaction mechanism of these two phenomena has rarely been reported due to the complicated tribo-dynamic behaviour [2,3]. The comprehensive investigation cooperating both the vibration and the wear mechanism is necessary for the prediction of early failures caused by the skidding in pure rolling contact.

Theoretical models have been developed for understanding the skidding behaviour of rolling bearings. These quasi-static/dynamic models were first used for steady-state analysis of skidding behaviour. Based on the raceway control technique and quasi-static method, a skidding prediction model was developed for high-speed roller bearings by considering the friction between rolling elements and raceways [4]. The dynamic slips between the balls and raceways, under both axial and radial loads, were also evaluated by judging the skid criterion [5]. However, since dynamic loads are applied to the bearing, the contact between the tribo-pairs inevitably becomes discontinuous. Therefore, the development of fully dynamic models has received much attention in the current literature. For example, a dynamic contact model was

constructed to study the sliding between the rollers and raceways using the finite element method [6]. Another dynamic model was proposed to evaluate the skidding behaviour during bearing acceleration [7]. Furthermore, by considering the time-variable load conditions, a nonlinear dynamic model for the skidding analysis of cylindrical roller bearings was reported [8]. These researches have provided complete dynamic skidding models and laid the theoretical foundation for the analysis of rolling bearing vibration characteristics.

Driven by fault diagnosis requirements, the skidding models have been applied in the vibration response analysis of rolling bearings to improve the identification accuracy of the fault characteristic frequency. In particular, the skidding effect is regarded as a random variable in the analysis of defective bearing vibration characteristics [9]. A raceway defect model that considered the relative slippage of rolling bearings was developed for calculating the ball passing frequencies [10]. In another investigation, the localized defects on raceways were also analysed from the vibration responses of a cylindrical roller bearing [11]. Furthermore, the characteristic frequency of some skidding damages under the time-varying slip ratios and surface roughness was identified from the dynamic response of an angular contact ball bearing [12,13]. It can be generalized that the skidding vibration is inter-related with the speed, radial load, friction and wear of a rolling bearing. However, the generating mechanism of the vibration induced by the sliding-rolling contact has not been fully explored so far.

In the view of tribological performances, the influences of sliding-rolling contacts on the wear, friction and lubrication were

---

* Corresponding author.
E-mail address: wt-h@163.com (T. Wu).

investigated. With a double roller tester to simulate the sliding-rolling contact, the tribological performance of the M50 bearing steel under extreme conditions was evaluated to ascertain the ultimate capacity and failure of sliding-rolling contact surfaces [14]. The surface asperities plastic deformation was examined to manifest the wear evolution under sliding-rolling friction [15,16]. The transient temperature field distribution characteristics, the thermal effect, in sliding-rolling contact were examined by the finite element method [17]. To consider the effects of the lubrication mechanism, the variation dependence was formulated for the oil film thickness in the contact area of the roller and inner ring by using the ultrasonic testing method [18]. It can be generalized that in most studies, the above influences are investigated separately rather than a comprehensive analysis. Besides, the interacting mechanism among the wear failure, vibration, and sliding-rolling friction has not been fundamentally elucidated.

So far, the sliding-rolling contact has attracted increasing interests and has been studied with different focuses. Concerning the dynamic behaviour, it is treated as the excitation of vibration. While in the view of tribological performances, it is considered as the source of wear. Essentially, the vibration induced by the skidding in rolling contact is a tribo-dynamic phenomenon in the contact interface. However, with the absence of knowledge on the interaction mechanism, the failure cannot be comprehensively predicted based on both the vibration and the wear [2,3].

To address this issue, the current work focuses on an experimental and numerical investigation on the tribo-dynamic responses of a simplified sliding-rolling contact, and explores the vibration mechanism by considering the vibration frequency, contact stress and wear. Specifically, the vibration frequency analysis is carried out by varying the slip ratio of the sliding-rolling contact. Furthermore, a surface contact stress analysis is conducted to reveal the contact mechanism in the sliding-rolling contact. Finally, the surface topography and oil debris analyses are carried out for wear detection.

The rest of the paper is organized as follows. In Section 2, the analysis of vibration frequency under sliding-rolling contact is presented. Section 3 details the analysis of surface contact stress. The identification of wear characteristics is given in Section 4. Finally, conclusions are given in Section 5.

2. Vibration frequency analysis under sliding-rolling contact

Occasional skidding in a rolling bearing is arduous to be precisely measured because it often accompanies other kinds of motions. To focus on skidding, a simplified sliding-rolling tribo-pair is adopted in this work. With two independently driven tribo parts, the sliding-rolling can be well controlled and the friction and wear can be easily assessed. Although this is an approximation to a real bearing, it is reasonable for qualifying the sliding-rolling tribological behaviour of some key mechanical components. These include bearings, gears and wheel/rails [19–22].

A roller-ring tribo-pair is built with a real ring and profiled roller from the object bearing. Moreover, wide range conditions for the fundamental sliding-rolling phenomena are considered and not limited to a bearing. Time-Frequency analysis is conducted to explore the
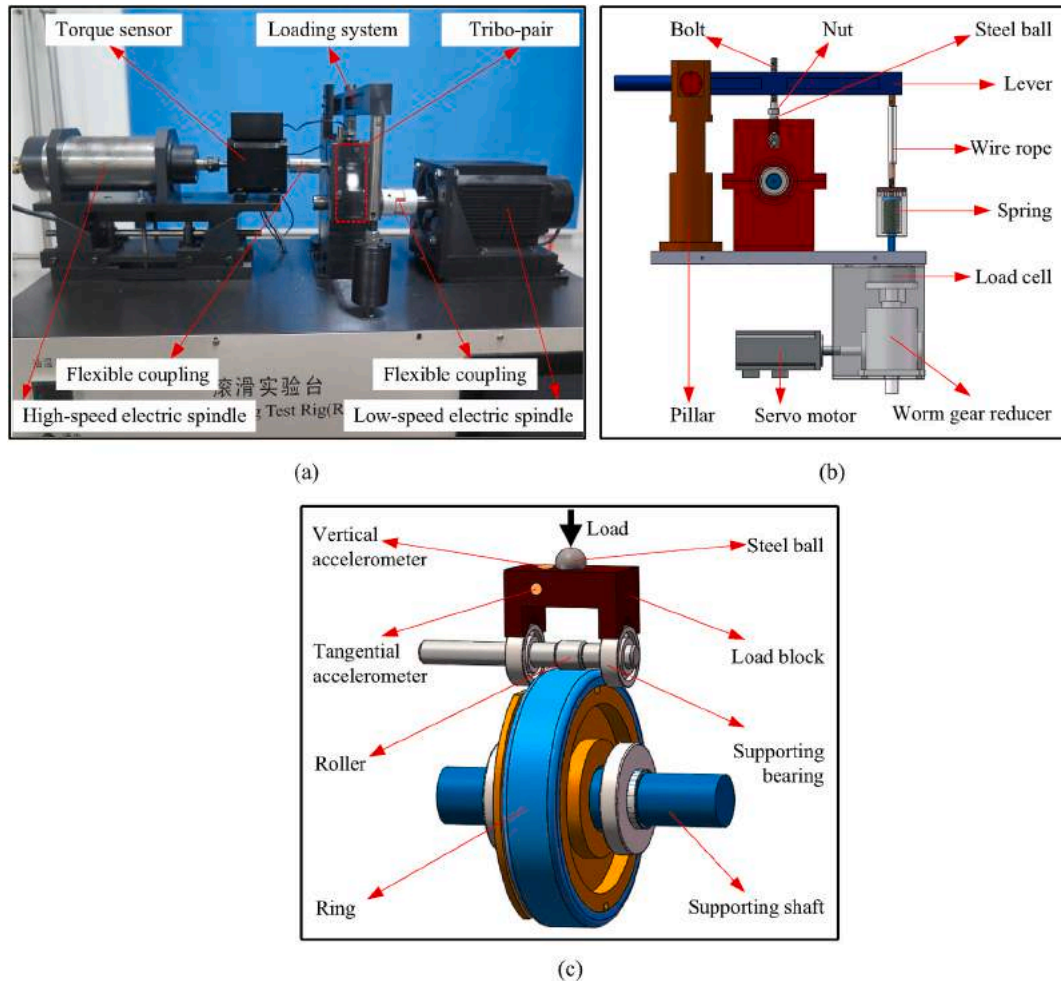

Fig. 1. The schematic diagram of the roller-ring test rig, (a) the physical system, (b) the principle of the loading system, (c) the detailed structure of the tribo-pair.

vibration characteristic frequency for different slip ratios. Afterwards, a simplified finite element model of the tribo-system is built to investigate the vibration characteristic under sliding-rolling contact.

2.1. Experimental details

2.1.1. Experimental apparatus

As shown in Fig. 1, the roller-ring tribo-system is employed for friction and loading tests. Referring to the *NU209EM* bearing, the $\varphi12$ mm roller is profiled with an additional holding section and the $\varphi108$ mm ring is directly dismantled from the bearing. The roller is driven by a high-speed electric spindle with a flexible coupling to isolate the radial impact from the driver and the ring is fixed on a low-speed electric spindle, as can be seen in Fig. 1(a). Sliding-rolling motions are obtained by setting different drive speeds.

The principle of the loading system and detailed structure of the tribo-pair are shown in Fig. 1(b) and (c) respectively. The ring is positioned by the supporting shaft and the roller is in contact with the ring through two supporting bearings. The loading system is mainly composed of the pillar, lever, load block, wire rope, spring, load cell, worm gear reducer and servo motor. In the test, one end of the lever is connected to the pillar and the other end is pulled by the wire rope driven by the servo motor. A bolt and a nut are fixed on the lever to apply the vertical load to the load block, supporting bearings and then to the tribo-pair. To avoid the unbalanced loading, a steel ball is set on the block to transfer the load. The load is applied by controlling the speed of the servo motor and measured by the load cell connected with the spring and the worm gear reducer.

Two accelerometers that sense the vertical and tangential vibrations are fixed on the load block. In this configuration, the vertical direction is the loading direction and the tangential direction is the rotational direction. A torque sensor that connects the high-speed electric spindle and roller is employed to measure the friction force in the rotational direction.

2.1.2. Experimental conditions

The slip ratio has been widely used to describe the slip phenomenon in sliding-rolling tribo-systems including bearings, gears and wheel/rails [17,20,23,24]. In this work, the slip ratio is adopted to evaluate the skidding degree:

$$s = 1 - (D_i N) / (D_r n)$$

where D_i and D_r are the diameters of the ring and the roller, N and n are their corresponding rotational speeds [17,23].

To study the influence of sliding-rolling contacts on vibration characteristics, the slip ratios of 0–0.5 are applied and two groups of sliding-rolling experiments are carried out under the operating conditions shown in Table 1 and Table 2.

Experiment No. 1 aims to explore the range of vibration frequency induced by the sliding in rolling contact and it contains two steps that operate continuously without stopping the machine. Step 1 is carried out at the first 10 s and the slip ratio is set at 0 for a pure-rolling motion. Step 2 starts running at 11 s by increasing the roller speed rapidly, thus the slip ratio is changed to 0.2 to generate a sliding-rolling motion. Experiment No. 2 is carried out sequentially under slip ratios of 0, 0.1, 0.2, 0.3, 0.4, 0.5 and each step lasts for 60 s. The above experiments are conducted under a constant load of 200 N. To avoid the error caused by

Table 1
Operating conditions of experiment No. 1

Step	Slip ratio	Rotational speed (rpm)		Load (N)	Time (s)
		Ring	Roller		
1	0	200	1800	200	10
2	0.2	200	2250	200	10

Table 2
Operating conditions of experiment No. 2

Step	Slip ratio	Rotational speed (rpm)		Load (N)	Time (s)
		Ring	Roller		
1	0	200	1800	200	60
2	0.1	200	2000	200	60
3	0.2	200	2250	200	60
4	0.3	200	2571	200	60
5	0.4	200	3000	200	60
6	0.5	200	3600	200	60

different lubrication effects in the contact region, the experiments are carried out under no lubrication conditions. Moreover, the surfaces of the tribo-pair are cleaned with acetone before the test to eliminate the effects of contamination particles on the sliding motion. Both the vibration and friction force signals are acquired with a sampling frequency of 20 kHz.

2.2. Analysis and discussion

2.2.1. Time-frequency analysis

The measured vibration acceleration signals of experiment No. 1 in both the vertical and tangential directions are shown in Fig. 2. The original acceleration signals are preprocessed by removing the mean. Fig. 2(a) indicates that from the pure-rolling to the sliding-rolling stage, the vertical acceleration amplitude increases from ± 2 m/s^2 to ± 5 m/s^2 and the tangential acceleration amplitude increases from ± 1 m/s^2 to ± 2 m/s^2 as shown in Fig. 2(b). It can be concluded that when the relative sliding occurs, the vibration energy in both the vertical and tangential directions increases accordingly.

Due to the instantaneous motion transition from pure-rolling to sliding-rolling, the time-frequency analysis is conducted by using a short-time Fourier transform. The corresponding time-frequency spectrum is shown in Fig. 3.

Fig. 3(a) indicates that the vertical vibration of the pure-rolling stage is mainly distributed in two frequency bands, including 2000–4000 Hz and 6000–7000 Hz. But when sliding-rolling motion occurs, there is no significant change in the vibration spectrum except that for the signal energy increases in these two frequency bands. For the tangential vibration, the global signal energy is relatively weaker, as shown in Fig. 3 (b). The vibration frequencies are distributed in the entire frequency range and there are no dominant peaks, which is a typical characteristic of friction-induced vibration signals [25–27]. Existing researches have also shown that the friction vibration signals are weak signals with low energy and there is no obvious natural frequency in the frequency spectrum [25].

Besides, it can be seen from Fig. 3(b) that, when sliding-rolling motion occurs, the characteristic frequencies within 0–1000 Hz appear which are almost absent in the pure-rolling stage. These frequencies can be considered to be induced by the sliding-rolling friction contact between the tribo-pair. Therefore, the vibration frequencies induced by the sliding movement in rolling contact are mainly the tangential vibration frequencies of 0–1000 Hz.

2.2.2. Tangential vibration frequency analysis under different slip ratios

According to the above analysis, the tangential vibration signals obtained in experiment No. 2 are extracted for further frequency analysis. The time-domain signals under different slip ratios and their corresponding frequency-domain signals in 0–1000 Hz are shown in Fig. 4. In order to identify the frequency components accurately, a five-spot triple smoothing method is used to eliminate the irregularity and interference. The main characteristic frequencies of each frequency spectrum are marked in red.

Fig. 4 shows that the vibration amplitude increases gradually with the increase of the slip ratio. This is because higher friction-induced
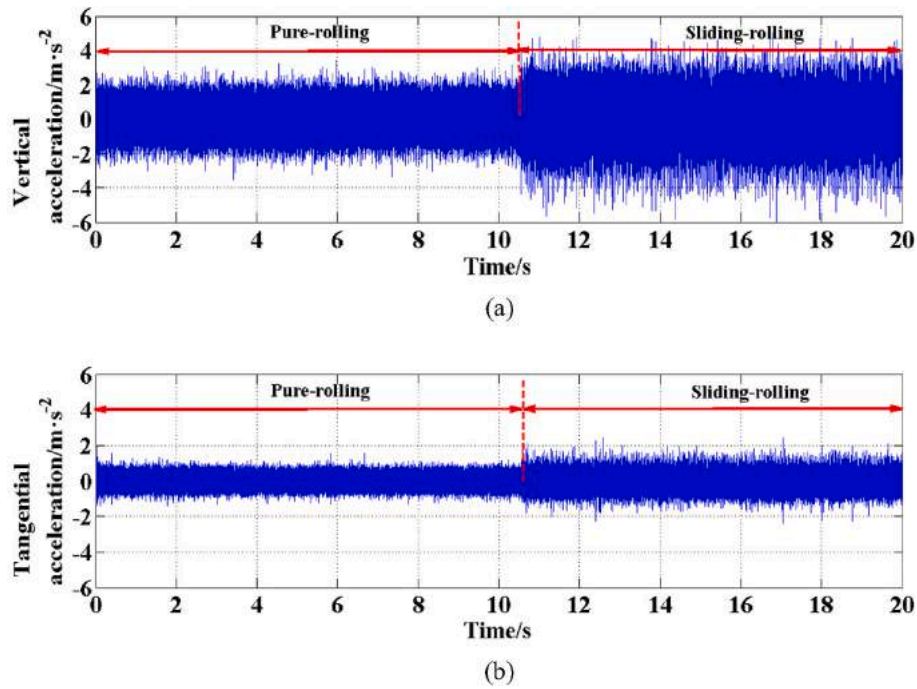
Fig. 2. The time history of vibration signals, (a) vertical vibration, (b) tangential vibration.
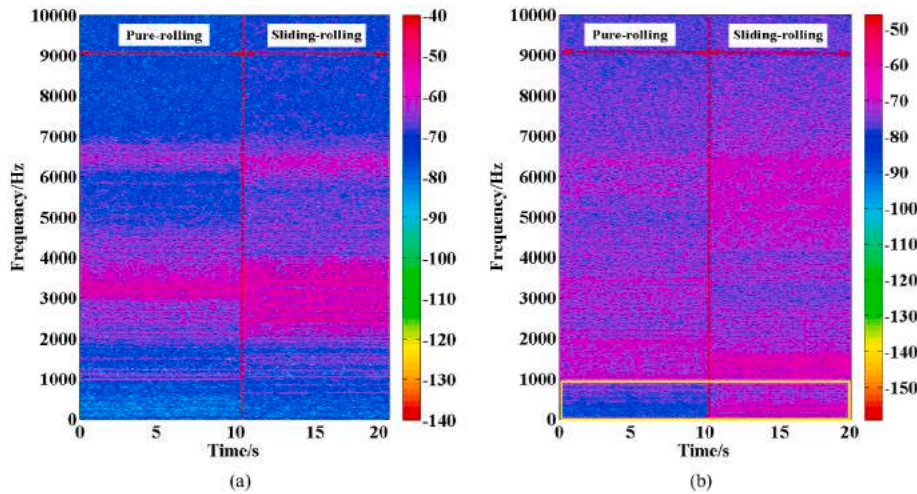

Fig. 3. The time-frequency spectrum of vibration signals, (a) vertical vibration, (b) tangential vibration.

vibration energy is excited due to the increase in the relative sliding velocity. As marked in each frequency spectrum, the corresponding first-order vibration frequencies are 30, 31, 35, 40, 47 Hz and 57 Hz. According to the experimental conditions in Table 2, the corresponding rotational frequencies of the roller are 30, 33.3, 37.5, 42.85, 50 Hz and 60 Hz. The first-order vibration frequency is close to the rotational frequency of the roller. The deviations may be caused by the connecting parts in the torque transmission path. Therefore, the first-order frequency of the tangential vibration frequency spectrum can reflect the actual rotational speed of the roller. Besides, it can be seen from Fig. 4 that a large number of harmonics are excited, and the number of harmonics gradually increases as the slip ratio increases from 0 to 0.5.

To explain this phenomenon, the tangential vibration and friction force signals under a slip ratio of 0.2 are extracted for further analysis. Low-pass filters at 1000 Hz and 50 Hz cut-off frequencies are applied to the tangential vibration and friction force signals respectively. Then the filtered signals are partially expanded to analyse the motion state of the

tribo-pair under sliding-rolling contact, as shown in Fig. 5.

The original tangential vibration and friction force signals are shown in Fig. 5(a) and Figure (b). The filtered results are shown in Fig. 5(c) and (d), it can be seen that both vibration and friction force signals demonstrate periodic fluctuations. According to the enlarged views in Fig. 5(e) and (f), the pulse periods of vibration and friction force signals are the same except for small deviations on the time scale, which may be caused by the phase changes in the stage of signal acquisition and signal processing.

During the experiment, the tribo-pair has the motions of the self-rotation and the relative sliding simultaneously. It can be seen from Fig. 5(e) and (f), at the initial stage, the roller comes into contact with the ring and the static friction force reaches its maximum magnitude, as labelled by the point 'a' in the figure. At the moment of relative sliding, the static friction force vanishes and the contact evolves into a status dominated by dynamic friction force, such that the roller vibrates near the equilibrium position. Affected by the system structure, surface
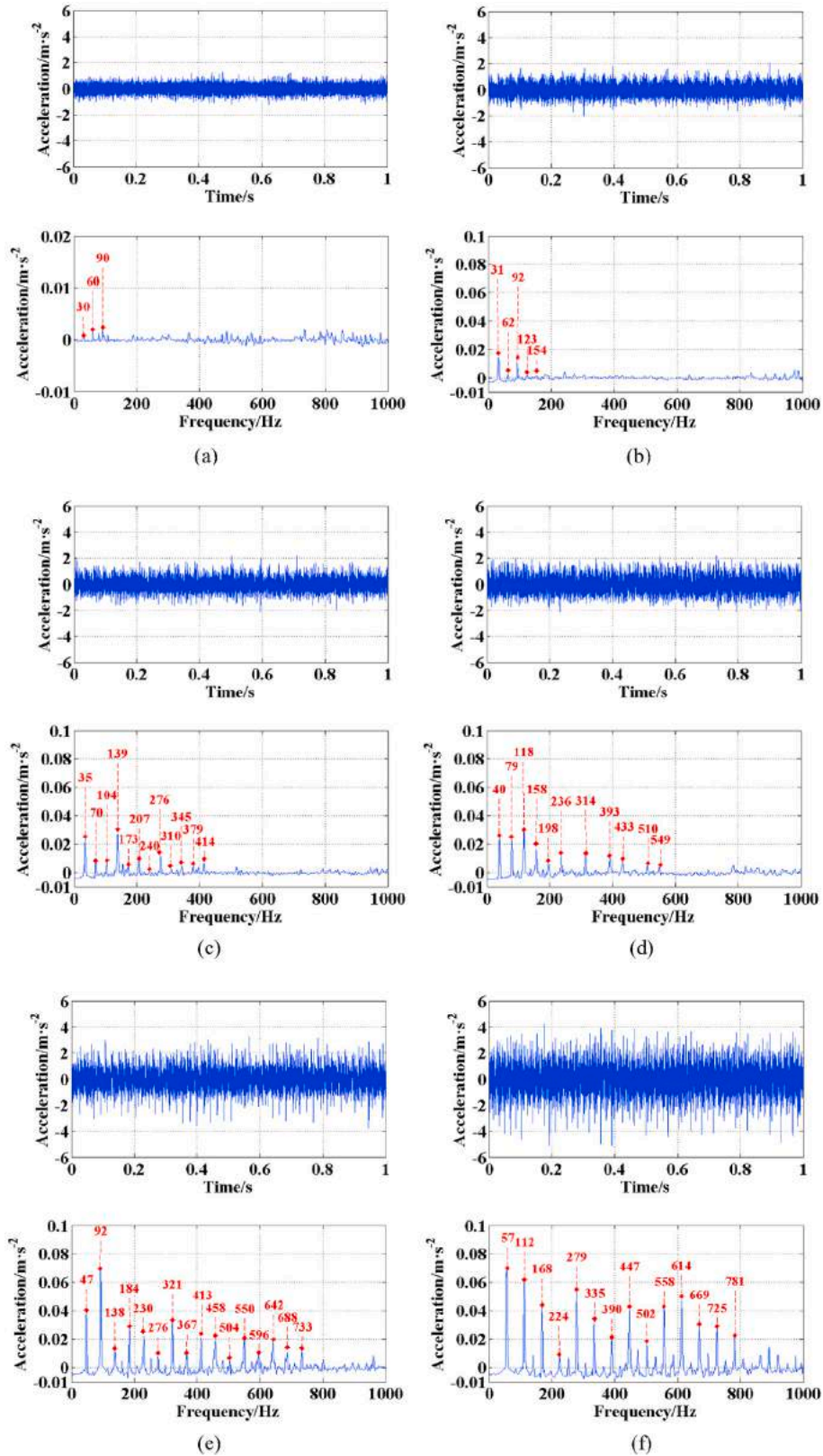
Fig. 4. Time-domain and frequency-domain diagrams of tangential vibration under different slip ratios, (a) slip ratio 0, (b) 0.1, (c) 0.2, (d) 0.3, (e) 0.4, (f) 0.5.

roughness, and other factors, the relative sliding speed is gradually reduced, resulting in a decrease of friction force and vibration, as indicated by the point 'b'. The friction force increases again until the two surfaces come into contact, as indicated by the point 'c'. The cycle period corresponds to the rotational frequency of the roller. On the other hand,

due to the non-linear changes of factors such as surface morphology and contact pressure, the irregular waveform in vibration signals is caused, as indicated by the points 'a' to 'd' in Fig. 5(e), and thus the harmonics are generated in the tangential vibration frequency spectrum [28].

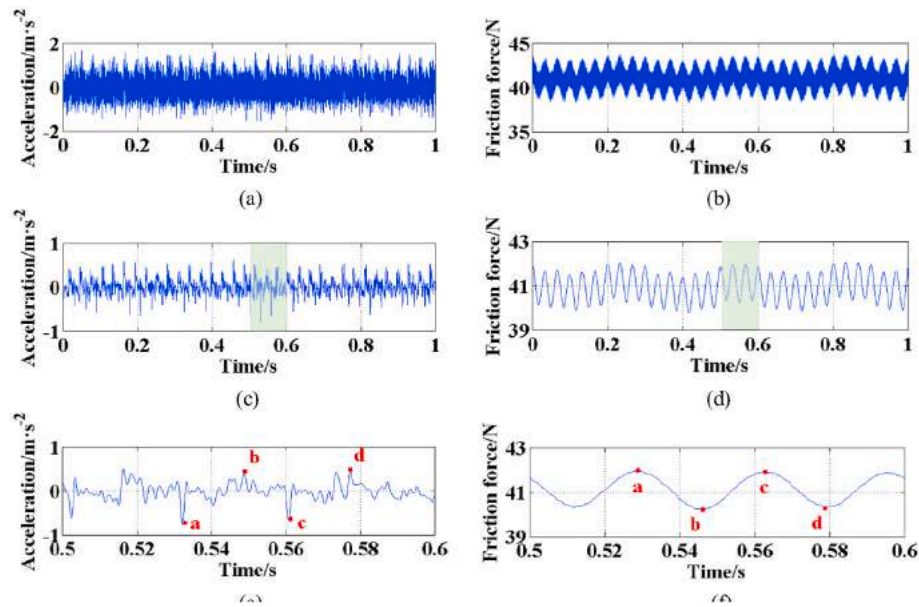The above analysis process is consistent with the classical stick-slip

Fig. 5. Tangential vibration and friction force signals under slip ratio 0.2, (a) and (b) original signals, (c) and (d) filtered signals, (e) and (f) partially amplified signals.

motion, which has widely used to explain the friction vibration mechanism [29]. This analysis result shows that the tangential vibration signal, introduced by sliding-rolling contact, contains the rotational frequency of the roller and its higher harmonics.

2.3. Finite element simulation

A numerical simulation is performed to verify the above vibration characteristics by using the explicit dynamic finite element code ABAQUS/Explicit. This analysis procedure is commonly used for solving nonlinear problems without considering the iteration and convergence criteria. It is based on the implementation of an explicit central-difference time integration rule together with the use of diagonal lumped element mass matrices. It can evaluate the normal and tangential contact stresses along the contact region [30,31]. Thus, the friction effect between the roller and ring can then be fully considered in the analysis. A simplified finite element model, as shown in Fig. 6, is created according to the geometry of the experimental system.

Fig. 6(a) shows the components of the finite element model. The ring is fixed to the supporting shaft and the roller shaft is attached to the

drive shaft. The two supporting bearings are simplified as two ferrules with their upper parts cut into planes and tied with the load block. Based on the experimental measurement, a friction coefficient between the roller and ring is set to 0.2. The roller shaft and the supporting bearings are assumed to be in friction contact with a friction coefficient of 0.01. All the contact surfaces in this model are considered perfectly flat and the thermal effects are neglected. Material properties of the parts used in the numerical calculation are based on their actual values, as listed in

Table 3
Material properties of the parts in finite element model.

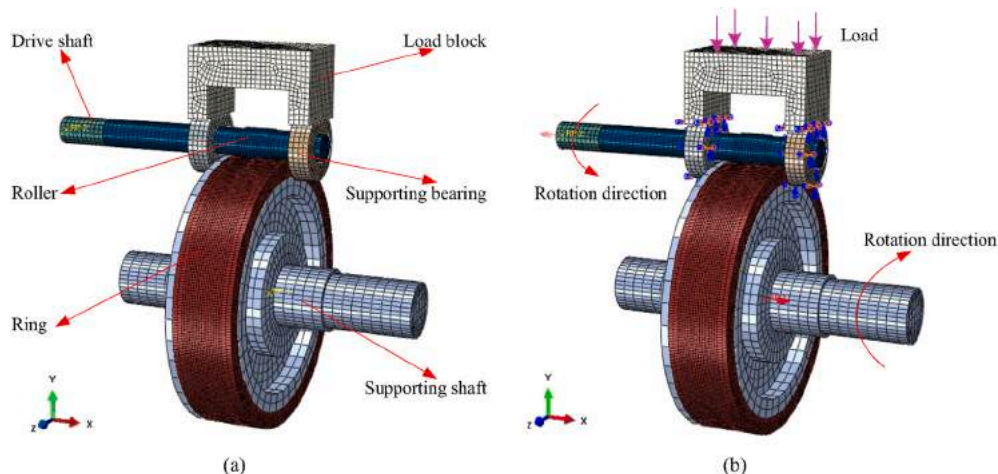| Part	Density (kg/m³)	Young's modulus (GPa)	Poisson's ratio
Drive shaft	7820	210	0.288
Roller	7800	207	0.3
Ring	7800	207	0.3
Load block	7850	210	0.31
Supporting bearing	7800	207	0.3
Supporting shaft	7850	210	0.31

Fig. 6. The finite element model of the tribo-system, (a) components of the model, (b) load and boundary conditions of the model.

Table 3.

The load and boundary conditions of the model are shown in Fig. 6 (b). The rotational velocity boundary conditions are applied to the supporting shaft and the drive shaft in the x-direction. The normal load is applied to the block in the y-direction. Other constraint conditions are all consistent with the real experimental system. In the dynamic analysis, the element type used is C3D8R, the contact formulation is the kinematic method with the finite sliding formulation and the friction formulation is the penalty method.

The total simulation duration is 0.502 s. At the first stage (0–0.001 s), a normal load of 200 N is applied and then keeps constant. At the second stage (0.001–0.002 s), a pure-rolling motion and a sliding-rolling motion with a slip ratio of 0.2 are performed respectively under the same operating conditions as the experiments. At the last stage (0.002–0.502 s), the results are obtained.

2.4. Analysis of the simulation results

According to the experimental results, the vibration frequencies induced by sliding-rolling contact are in the range of 0–1000 Hz. Therefore, the tangential displacement signal, which is more accurate for low-frequency characteristics analysis, is extracted for spectrum analysis. The frequencies above 1000 Hz are filtered to accurately identify the characteristic frequencies induced by sliding-rolling friction, as shown in Fig. 7.

As can be seen from Fig. 7(a) and (b), the time-domain signals under sliding-rolling contact show the larger amplitude and obvious periodic impulses, which are highly consistent with the filtered result in Fig. 5(c). It verifies that the motion state of the tribo-pair changes periodically between relative static and relative sliding as described in Section 2.2.2.

Fig. 7(c) and (d) show the frequency-domain analysis results. The main characteristic frequencies are marked in red. According to these annotations, the first-order frequencies under pure-rolling and sliding-rolling contact are 30 Hz and 38 Hz respectively, which exactly correspond to the roller speed of 1800 rpm and 2250 rpm in the simulation.

Besides, it can be seen from Fig. 7(c) and (d) that, the higher harmonics are excited both in the frequency-domain diagrams of pure-rolling and sliding-rolling motion. Also, the harmonic amplitude under sliding-rolling contact is greater than that under pure-rolling contact. It is due to the large friction force caused by sliding-rolling contact, more vibration energies are excited than the pure-rolling condition. The

harmonics amplitude also depends on such nonlinear factors such as system damping, load, lubrication state, surface morphology, material characteristics, and these influences are neglected in this study.

The above experiment and simulation results reveal that the tangential vibration frequencies are highly synchronized with friction contact variation and simultaneously varied with the roller speed. In practical applications of rolling bearings, the inner ring speed is usually fixed and the roller speed is unknown, which makes it difficult to accurately evaluate the degree of skidding. Currently, various advanced sensing technologies are applied to online monitor the skidding of bearings. The eddy-current, optical fibre, ultrasonic sensors are used to monitor the cage speed of bearings and thus to evaluate the skidding degree [32–34]. The wireless temperature sensors can detect the inner or outer ring temperature rise caused by skidding [35]. However, these sensors need to be installed on bearings and even need to change the original structure of bearings, which is still a difficulty to realize for the extreme working environment and limited space of rolling bearings. The relative sliding between the roller and inner ring is an important excitation to the vibration of rolling bearings. Therefore, according to the vibration characteristics of sliding-rolling contact, the roller speed can be obtained and thus can provide valuable information for skidding detection.

3. Surface contact stress analysis

The vibration frequency analysis indicates that the dynamic behaviour under sliding-rolling contact is determined by the contact property between the tribo-pair. To explore this contact mechanism, a two-dimensional finite element model is constructed and the surface contact stress analysis is performed by using ABAQUS/Explicit.

3.1. Twin-discs finite element model

In order to reduce the meshing and calculation time, a simplified finite element model consisting of two $\varphi12$ mm discs is adopted in this work, as shown in Fig. 8. This simplification is different from that in the experiment. With the purpose of stress analysis, such simplification is reasonable because the contact stress in the current analysis maintains the equivalence with that of the experiment. Besides, the width of the contact area in the simulation model is much smaller than the equivalent radius of curvature [36]. Therefore, the influence of the simplification of
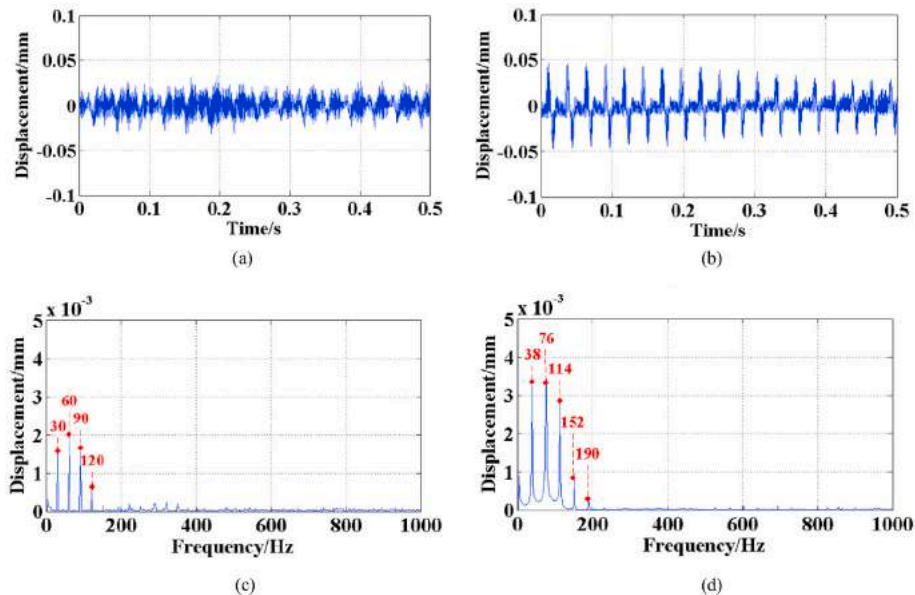

Fig. 7. Time-domain and frequency-domain signals of tangential vibration, (a) and (c) under pure-rolling contact, (b) and (d) under sliding-rolling contact.
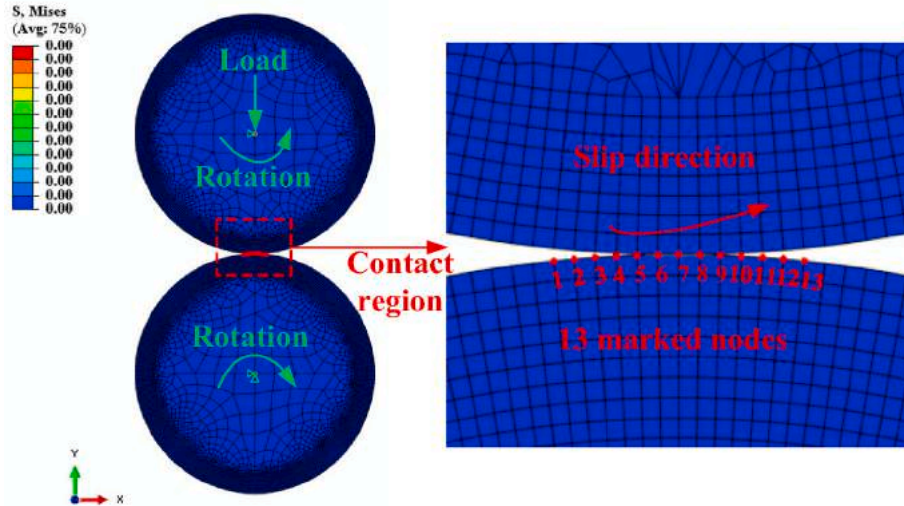
Fig. 8. The finite element model of twin-discs contact.

the geometry is limited in the current case.

The boundary conditions of the rotation and y-direction displacement are applied to the upper disc, and a normal load is applied to the centre. However, only the rotating boundary condition is applied to the lower disc. Two discs are in friction contact with a friction coefficient of 0.2 and the model is a mesh of CPS4R elements. The material property and contact conditions are the same as those described in Section 2.3.

The analysis is focused on the stress distribution of the contact region at the pure-rolling and sliding-rolling instants. Fig. 8 illustrates the contact region of two discs. The lower disc is selected as the research object. The 1–13 element nodes, of which the 7-node is positively the center, are marked as tracking targets in the contact region.

A pure-rolling motion and a sliding-rolling motion are simulated respectively. The entire analysis process consists of two stages. At the first stage (0–0.001 s), a normal load of 50 N is gradually applied and then keeps constant. Referring to the experimental conditions in Table 2, the applied load should be 200 N (the corresponding maximum contact stress is 334 MPa calculated by Hertz contact theory). However, for the simplified two-dimensional twin-discs model, to maintain the approximate maximum stress, the applied load in the model is calculated as 50 N. At the second stage (0.001–0.002 s), a rotational speed of 1800 rpm is applied on the two discs to simulate a pure-rolling motion. The upper disc speed is changed to 2250 rpm to simulate the sliding-rolling motion at a slip ratio of 0.2.

3.2. Contact stress analysis

The von Mises stress distribution in the contact region at different times is shown in Fig. 9. Among them, 0.001 s and 0.0012 s refer to the instants before and after the pure-rolling or sliding-rolling motion, respectively. Fig. 9(a) and (b) show that the stress distribution has not changed significantly when pure-rolling occurs. The stress at the central node is concentrated and diffused uniformly around it. However, the stress concentration points of the two discs are asymmetrical and offset when sliding-rolling occurs, as shown in Fig. 9(c).

To further investigate the contact stress change, the normal stress S22 and shear stress S12 of the 13 nodes in the contact region are extracted, as shown in Fig. 10. It can be seen from Fig. 10(a) and (c) that the normal stress of node-7 is the largest at 0.001 s, while the shear stress is zero. Due to elastic deformation, nodes on both sides of the node-7 are subjected to positive and negative shear stresses respectively. Among them, shear stresses at node-6 and node-8 are the largest and show a symmetrical distribution. Fig. 10(b) shows that the normal stress distributions are the same when pure-rolling and sliding-rolling motion occurs, while their shear stress distributions show a clear difference, see Fig. 10(d).

When pure-rolling motion occurs, the shear stresses at node-5 and node-7 are exactly the same except for the direction. However, the shear stress at node-5 decreases while the shear stress at node-7 increases sharply when sliding-rolling motion occurs. This is because the relative
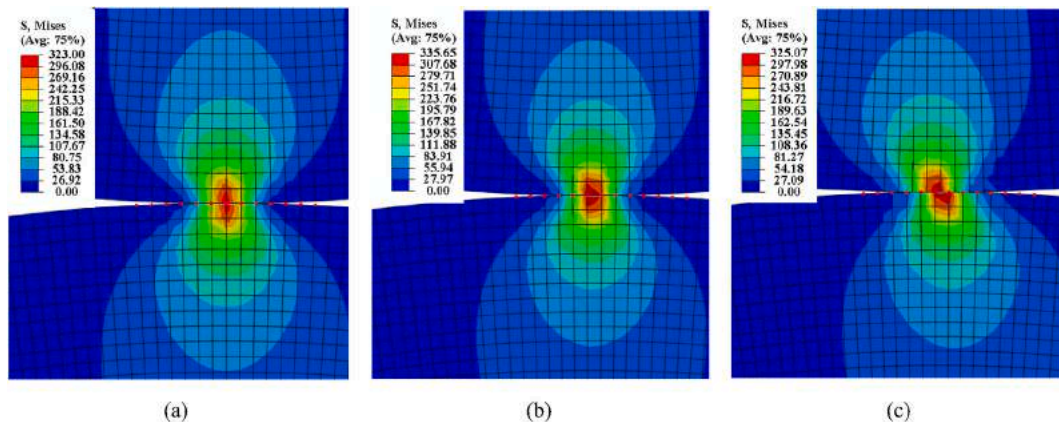

Fig. 9. The von Mises stress distribution in the contact region, (a) at 0.001 s, (b) at 0.0012 s of the pure-rolling motion, (c) at 0.0012 s of the sliding-rolling motion.
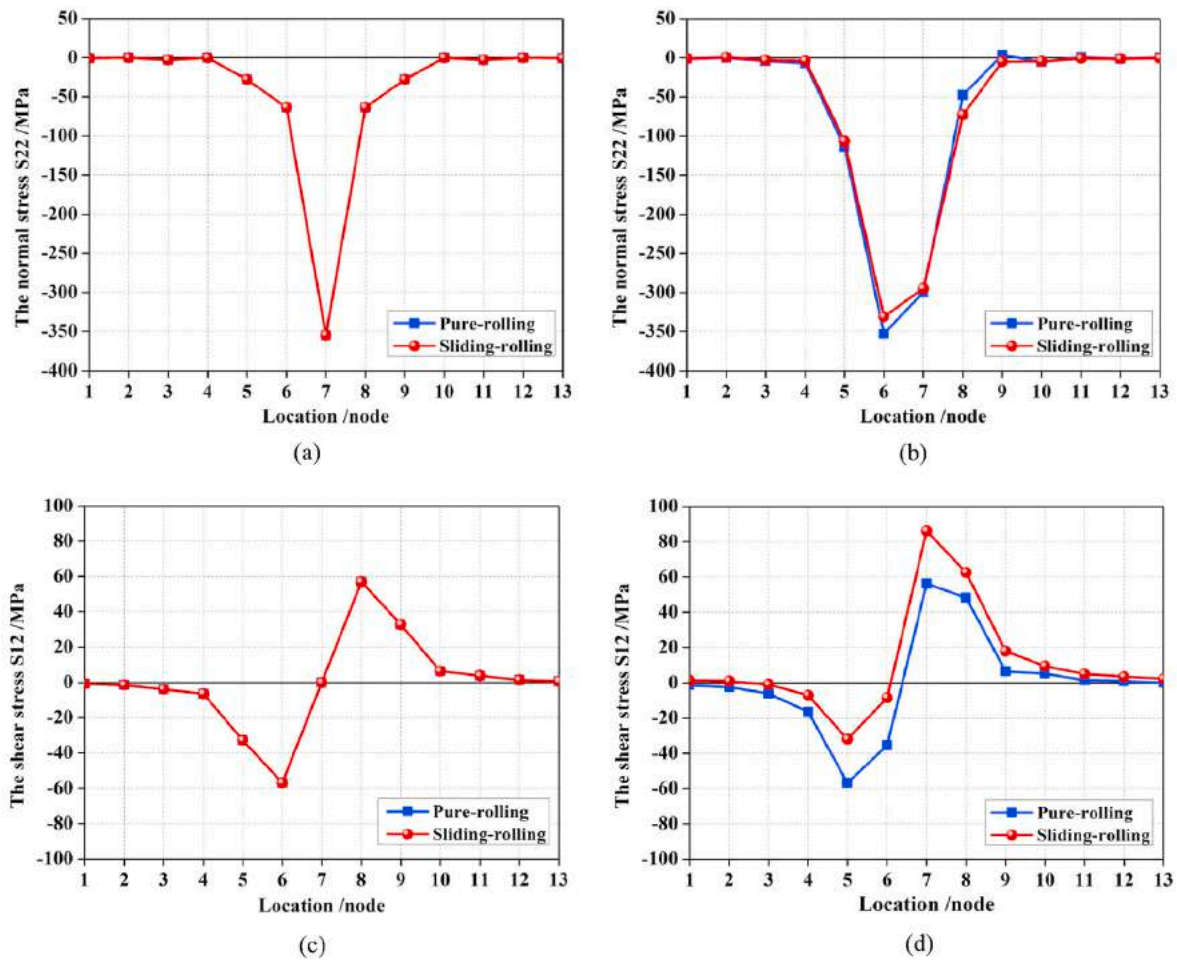
Fig. 10. The nodal stress distribution, (a) the normal stress S22 at 0.001 s, (b) the normal stress S22 at 0.0012 s, (c) the shear stress S12 at 0.001 s, (d) the shear stress S12 at 0.0012 s.

sliding between two discs has made nodes, on the right side of node-7, subject to the extrusion of the upper disc. Thus, the elastic deformation is increased while the elastic deformation near 5-node quickly recovers.

The shear stress variation of sliding-rolling contact show that when two discs slide relatively, the external force consists of the normal force and friction force, causing the contact interface deformation. To resist such elastic deformation, an increased shear stress is generated, accompanied by changes in the position of the maximum stress point.

Combining the shear stress variation in Fig. 10 and the friction contact process in Fig. 5, the sliding-rolling contact shows similar contact mechanism with the stick-slip motion. According to the stick-slip theory [37,38], there are two motion regimes between two relative sliding bodies. At the initial stage of relative sliding, the two bodies are in a stick motion as the static friction force, elastic deformation and shear stress gradually increase. It becomes a slip motion when relative sliding generates between the two bodies. This process occurs repeatedly, resulting in stick-slip vibration.

Based on the stick-slip theory, the relationship between the contact deformation and vibration behaviour is analysed in previous studies. The effects of contact stiffness on stick-slip vibration are studied and results show that increasing the stiffness leads to a reduction of the elastic deformation and vibration amplitude [39]. The deformation of contact interfaces is proved to be the main reason for the stick-slip vibration through wear morphology analysis [40]. Therefore, for sliding-rolling contact, the unstable shear stress variation due to the elastic deformation of contact interfaces may be the root cause of

tangential vibration generation.

4. Wear characteristics identification

In order to analyse the wear failure under sliding-rolling contact, long-term wear tests are carried out on the roller-ring test rig and wear checks are conducted through surface topography and wear debris analyses. The tests are performed under oil lubrication conditions. The lubricating oil is injected into the contact region driven by a peristaltic pump and then returns to the oil cup. Before each test, the oil cup is cleaned with acetone and filled with 500 ml new lubricating oil. The lubricating oil used in this experiment is the base oil without any additives. The operation conditions are shown in Table 4.

4.1. Surface topography analysis

The surface topographies of the ring that are observed by an optical

Table 4
Operating conditions of the wear tests.

Motion	Slip ratio	Rotational speed (rpm)		Load (N)	Lubrication (ml/min)	Time (hr)
		Ring	Roller			
Pure-rolling	0	300	2700	500	20	10
Sliding-rolling	0.4	300	4500			

microscope, before and after the tests, are shown in Fig. 11. It can be seen from Fig. 11(a) that the fine finishing makes a relatively uniform roughness on the initial surface. Moreover, the worn surface under pure-rolling contact has no significant change after 10 h of wear test, see Fig. 11(b). Fig. 11(c) and (d) show that a large number of ploughs and scratches appear on the worn surface of different positions, which are typical characteristics of abrasive wear and adhesive wear [36]. This can be attributed to the break-down of the lubrication oil film under the local high temperature. Furthermore, the shear behaviour occurs between surface asperities during the sliding process.

4.2. Wear debris analysis

An On-line Visible Ferrograph (OLVF) [41] is used for online wear debris image acquisition. The OLVF oil suction tube is inserted into the oil cup to extract oil samples and wear debris images are captured every 2 min during the test. More than 300 wear debris images are collected for each test and three typical images are selected for wear analysis, as shown in Fig. 12. Fig. 12(a–c) and Fig. 12(d–f) are the wear debris images obtained during the pure-rolling and sliding-rolling experiment respectively and captured at the 3rd, 6th, and 9th hours of each test. Fig. 12(a–c) indicate that there are small wear particles produced under pure-rolling contact while much more wear particles with the larger volume and irregular shape are generated under sliding-rolling contact, see Fig. 12(d–f).

Existing researches on wear debris identification and classification divide the wear debris into five types: normal wear debris, spherical wear debris, cutting wear debris, fatigue wear debris and severe sliding wear debris [42]. Due to different generating mechanisms, each type of wear debris shows different shapes, surface textures, and edge information. In this work, a preliminary wear mechanism analysis is made according to the wear debris size and shape features. The wear debris produced during the pure-rolling wear test are all less than 20 μm in size and can be judged as normal wear debris. The slender wear debris produced during the sliding-rolling wear test have a length of 30–60 μm. Some of them show an obvious curved shape that is a typical feature of cutting wear debris and the formation mechanism is mainly the abrasive wear caused by the shear action in the sliding-rolling process. The large irregular wear debris with a length of more than 70 μm are identified as severe sliding wear debris. The generation mechanism is the excessively high shear stress produced by the relative moving surfaces due to excessive load and speed [43]. Therefore, the wear debris analysis results further reveal the shear effect of contact interfaces under sliding-rolling contact.

5. Conclusion

The vibration mechanism of sliding-rolling contact has been investigated experimentally and numerically. The tribo-dynamic responses including vibration frequency, contact stress, and wear are examined. The vibration frequency analysis is first carried out by varying the slip ratio on a roller-ring test rig, and the corresponding numerical
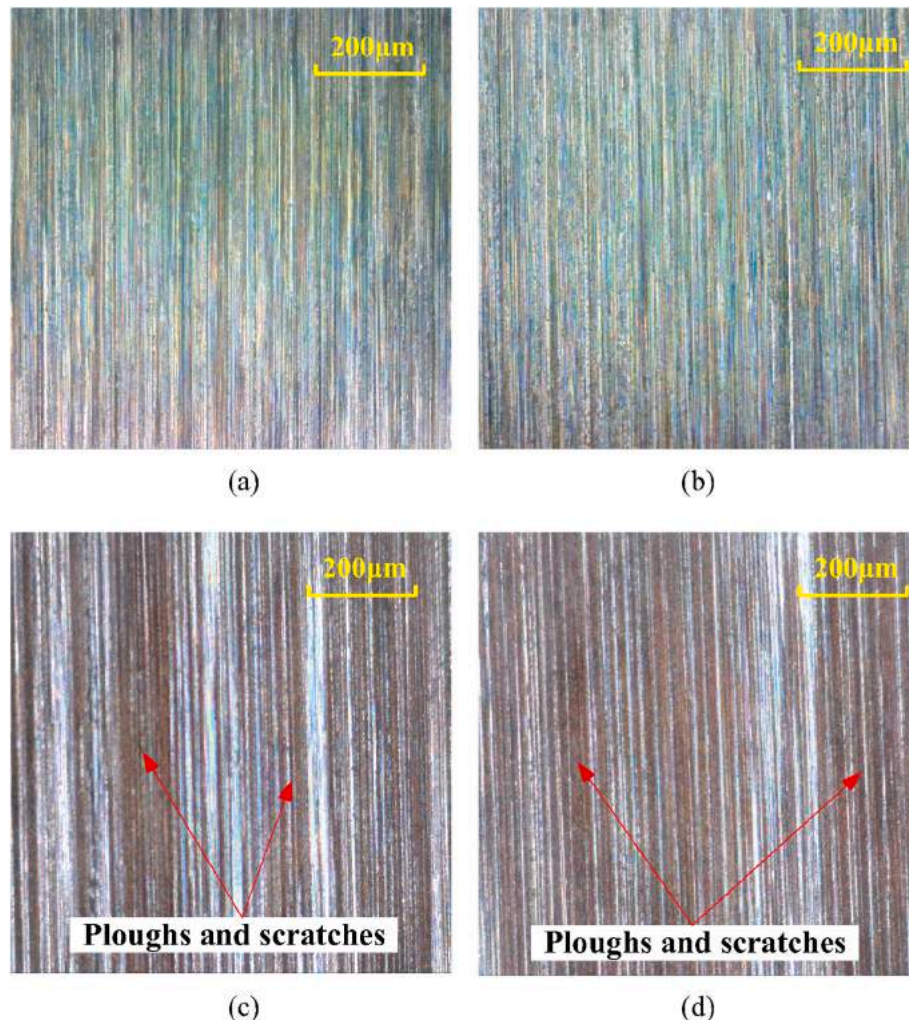

Fig. 11. Surface topographies of the ring, (a) initial surface, (b) after pure-rolling wear test, (c) and (d) after sliding-rolling wear test.
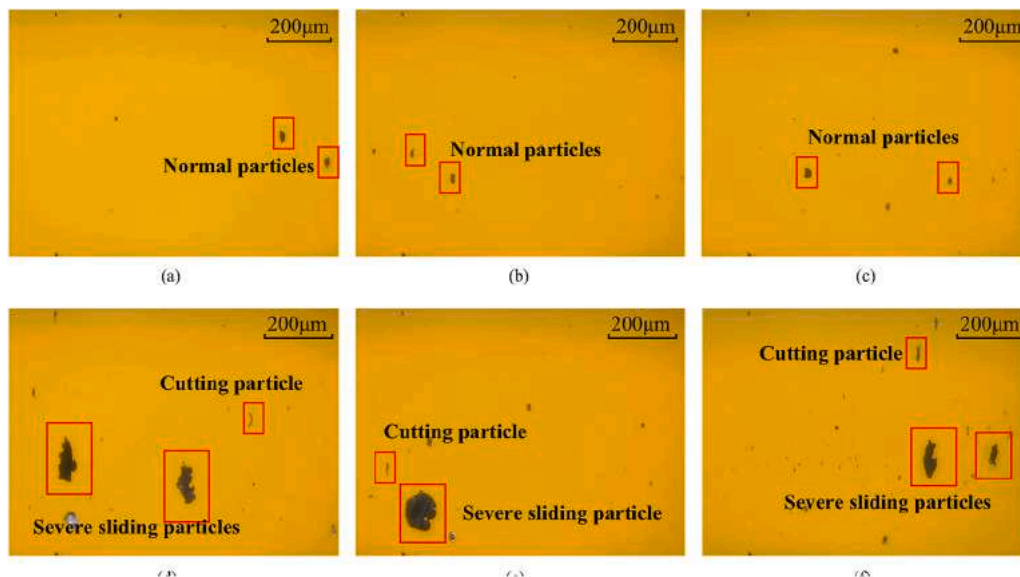
Fig. 12. Wear debris images captured, (a–c) at 3rd, 6th, 9th hours of pure-rolling test, (d–f) at 3rd, 6th, 9th hours of sliding-rolling test.

simulation is performed to verify the experimental results. Then, the surface contact stress analysis is performed by a twin-discs model to reveal the contact mechanism under sliding-rolling contact. Furthermore, surface topography and wear debris analyses are conducted for wear detection. The main conclusions can be summarized as follows:

(1) Sliding-rolling contact excites the tangential vibration frequencies composed of the rotational frequency of the roller and its higher harmonics, which are highly synchronized with the friction contact variation and simultaneously varied with the roller speed. This vibration characteristic may provide critical information for the skidding detection of rolling bearings.

(2) The surface contact stress analysis results show that, with the sliding occurring in rolling contact, the unstable shear stress change is induced due to the elastic deformation of contact area, which may be the root cause of tangential vibration generation. Further examinations on the wear scars and oil debris reveal that the wear failure under sliding-rolling contact coincides with the shear effect of contact interfaces.

CRediT authorship contribution statement

Chan Xu: Conceptualization, Methodology, Software, Validation, Formal analysis. **Tonghai Wu:** Resources, Supervision, Writing - original draft. **Hongbin Yang:** Investigation, Data curation. **Hongkun Wu:** Writing - original draft. **Ngaiming Kwok:** Writing - review & editing.

Declaration of competing interest

The authors declare that they have no known competing financial interests or personal relationships that could have appeared to influence the work reported in this paper.

Acknowledgement

References

[1] Wang YL, Wang WZ, Zhang SG, et al. Investigation of skidding in angular contact ball bearings under high speed. Tribol Int 2015;92:404–17.

[2] Bhardwaj V, Pandey RK, Agarwal VK. Experimental investigations for tribodynamic behaviours of conventional and textured races ball bearings using fresh and MoS2 blended greases. Tribol Int 2017;113:149–68.

[3] Ouyang TC, Huang GC, Chen JX, et al. Investigation of lubricating and dynamic performances for high-speed spur gear based on tribo-dynamic theory. Tribol Int 2019;136:421–31.

[4] Harris TA. An analytical method to predict skidding in high speed roller bearings. Tribol Trans 1966;9(3):229–41.

[5] Hirano F. Motion of a ball in angular-contact ball bearing. Tribol Trans 1965;8(4): 425–34.

[6] Laniado-Jácome E, Meneses-Alonso J, Diaz-López V. A study of sliding between rollers and races in a roller bearing with a numerical model for mechanical event simulations[J]. Tribol Int 2010;43(11):2175–82.

[7] Tu WB, Shao YM, Mechefske CK. An analytical model to investigate skidding in rolling element bearings during acceleration. J Mech Sci Technol 2012;26(8): 2451–8.

[8] Han QK, Li X, Chu FL. Skidding behavior of cylindrical roller bearings under time-variable load conditions. Int J Mech Sci 2017;135:203–14.

[9] Sawalhi N, Randall RB. Simulating gear and bearing interactions in the presence of faults Part II. Simulation of the vibrations produced by extended bearing faults. Mech Syst Signal Process 2008;22(8):1952–66.

[10] Niu LK, Cao HR, He ZJ, et al. A systematic study of ball passing frequencies based on dynamic modeling of rolling ball bearings with localized surface defects. J Sound Vib 2015;357:207–32.

[11] Wang F, Jing M, Yi J, et al. Dynamic modelling for vibration analysis of a cylindrical roller bearing due to localizes defects on raceways. Proc Inst Mech Eng - Part K J Multi-body Dyn 2015;229:39–64.

[12] Li JN, Chen WG, Xue JF, et al. Effect of multiple factors on identification and diagnosis of skidding damage in rolling bearings under time-varying slip conditions. Appl Sci Basel 2019;9(15):3033.

[13] Wang YL, Wang WZ, Zhang SG, et al. Effects of raceway surface roughness in an angular contact ball bearing. Mech Mach Theor 2018;121:198–212.

[14] Wang Liqin, Peng Bo, Gu Le, et al. Tribological performance of M50 steel triboparts. Tribol Trans 2012;55(2):191–8.

[15] Yusof NFM, Ripin ZM. A technique to measure surface asperities plastic deformation and wear in rolling contact. Wear 2016;s368–369:496–504.

[16] Xu C, Th Wu, Huo YW, et al. In-situ characterization of three dimensional worn surface under sliding-rolling contact. Wear 2019;426–427:1781–7.

[17] Li JN, Chen W, Xie YB. Experimental study on skid damage of cylindrical roller bearing considering thermal effect. Proc IME J J Eng Tribol 2014:1–11. 0(0).

[18] Zhang K, Meng QF, Chen W, et al. Ultrasonic measurement of oil film thickness between the roller and the inner raceway in a roller bearing. Ind Lubric Tribol 2015;67(6):531–7.

[19] Tian Y, He CG, Zhang J, Liu QY, Wang WJ. Experimental study on the vibration characteristic responses on the surface damage of wheel materials. Proc IME J J Eng Tribol 2018;232(9):1160–8.

[20] Stump BC, Zhou Y, Viola MB, et al. A rolling-sliding bench test for investigating rear axle lubrication. Tribol Int 2018;121:450–9.

[21] Ramalho A, Esteves M, Marta P. Friction and wear behaviour of rolling–sliding steel contacts. Wear 2013;302(1–2):1468–80.

[22] Zhou Y, Peng J, Wang WJ, et al. Slippage effect on rolling contact wear and damage behavior of pearlitic steels[J]. Wear; 2016. p. 78–86.

[23] Selvaraj A, Marappan R. Experimental analysis of factors influencing the cage slip in cylindrical roller bearing. Int J Adv Manuf Technol 2011;53(5–8):635–44.

[24] Seo JW, Jun HK, Kwon SJ, et al. Rolling contact fatigue and wear of two different rail steels under rolling-sliding contact. Int J Fatig 2016;83:184–94.

[25] Sun D, Li G, Wei H, et al. Experimental study on the chaotic attractor evolvement of the friction vibration in a running-in process. Tribol Int 2015;88:290–7.

[26] Immovilli F, Cocconcelli M, Bellini A, et al. Detection of generalized-roughness bearing fault by spectral-kurtosis energy of vibration or current signals. IEEE Trans Ind Electron 2009;56(11):4710–7.

[27] Lai VV, Chiello O, Brunel Jean-François, et al. Full finite element models and reduction strategies for the simulation of friction-induced vibrations of rolling contact systems. J Sound Vib 2019;444:197–215.

[28] Nadim AE, Hamzeh ZM, Montasser ST. Stick-slip detection through measurement of near field noise. [J]. J Mech Eng Res 2011, 3(3): 96-102.

[29] Ibrahim RA. Friction-induced vibration, chatter, squeal, and chaos—Part II: dynamics and modeling. Appl Mech Rev 1994;47(7).

[30] Wang DW, Mo JL, Ouyang H, et al. Experimental and numerical studies of friction-induced vibration and noise and the effects of groove-textured surfaces[J]. Mech Syst Signal Process 2014;46(2):191–208.

[31] Wang DW, Mo JL, Wang XF, Ouyang H, Zhou ZR. Experimental and numerical investigations of the piezoelectric energy harvesting via friction-induced vibration [J]. Energy Convers Manag 2018;171:1134–49.

[32] Liu ZX, Xu C, Li M, et al. Study on the rotational speed of bearing cage based on ultrasonic measurement. Proc Inst Mech Eng - Part K J Multi-body Dyn 2017;231 (4):684–9.

[33] Yan K, Yan B, Li BQ, et al. Investigation of bearing inner ring-cage thermal characteristics based on CdTe quantum dots fluorescence thermometry. Appl Therm Eng 2017;114:279–86.

[34] Du Y, Zhou SX, Jing XJ, Peng YP, Wu HK, Kwok NM. Damage detection techniques for wind turbine blades: a review[J]. Mechanical Systems and Signal Processing; 2019. 106445.

[35] Bashir I, Wang L, Harvey TJ. Integrated smart bearings for next generation aero-engines Part 1: development of a sensor suite for automatic bearing health monitoring [C]//. World Congress on Condition Monitoring, https://eprints.soton. ac.uk/id/eprint/411589; 2017. 12.

[36] Wen SZ, Huang P. Principles of tribology. Beijing: Tsinghua University Press; 2018.

[37] Wang XC, Huang B, Wang RL, et al. Friction-induced stick-slip vibration and its experimental validation[J]. Mechanical Systems and Signal Processing; 2020.

[38] McGuiggan Patricia M . Stick slip contact mechanics between dissimilar materials: effect of charging and large friction. Langmuir the Acs Journal of Surfaces & Colloids 2008;24(8):3970–6.

[39] Neis PD, Baets PD, Ost W, et al. Investigation of the dynamic response in a dry friction process using a rotating stick–slip tester. Wear 2011;271(9–10):2640–50.

[40] Dong C, Yuan C, Bai X, et al. Investigating relationship between deformation behaviours and stick-slip phenomena of polymer material. Wear 2017;376–377: 1333–8.

[41] Wu TH, Peng YP, Wu HK, et al. Full-life dynamic identification of wear state based on on-line wear debris image features. Mech Syst Signal Process 2014;42(1–2): 404–14.

[42] Raadnui S. Wear particle analysis—utilization of quantitative computer image analysis: a review. Tribol Int 2005;38(10):871–8.

[43] Yang QM. Wear particle analysis. Beijing: China Railway Press; 2002.